NANO LETTERS

Letter

pubs.acs.org/NanoLett

Hierarchical Nanoparticle Ensembles Synthesized by Liquid Phase Directed Self-Assembly

J. D. Fowlkes,*[,†] N. A. Roberts,[‡] Y. Wu,[§] J. A. Diez,[∥] A. G. González,[∥] C. Hartnett,[⊥] K. Mahady,[¶] S. Afkhami,[¶] L. Kondic,[¶] and P. D. Rack[†,§]

[†]Center for Nanophase Materials Sciences, Oak Ridge National Laboratory, Oak Ridge, Tennessee 37381, United States

[‡]Mechanical and Aerospace Engineering, Utah State University, Logan, Utah 84322, United States

[§]Department of Materials Science and Engineering, The University of Tennessee, Knoxville, Tennessee 37996, United States

[∥]Instituto de Física Arroyo Seco (CIFICEN-CONICET), Universidad Nacional del Centro de la Provincia de Buenos Aires, Pinto 399, 7000, Tandil, Argentina

[⊥]Department of Physics and Astronomy, The University of Tennessee, Knoxville, Tennessee 37996, United States

[¶]Department of Mathematical Sciences, New Jersey Institute of Technology, Newark, New Jersey 07102, United States

Supporting Information

ABSTRACT: A liquid metal filament supported on a dielectric substrate was directed to fragment into an ordered, mesoscale particle ensemble. Imposing an undulated surface perturbation on the filament forced the development of a single unstable mode from the otherwise disperse, multimodal Rayleigh–Plateau instability. The imposed mode paved the way for a hierarchical spatial fragmentation of the filament into particles, previously seen only at much larger scales. Ultimately, nanoparticle radius control is demonstrated using a micrometer scale switch.

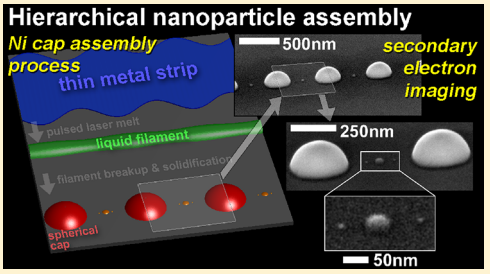

KEYWORDS: *Self-assembly, directed assembly, Rayleigh–Plateau, volume-of-Fluid, hierarchical, nanoparticle assembly*

Chemical synthesis methods provide means to produce high yields of metal nanoparticles with precise radii.[1] Magnetic moment,[2] surface tension,[3] and melting point[4] represent just a few material dependent properties that are drastically affected by metallic nanoparticle size in the sub-20 nm diameter range. Catalytic,[5] electrical,[6] and optical[7] applications stand to benefit from these size-dependent properties. However, approaches to pattern chemically synthesized nanoparticles on surfaces are fewer. As a result, physical-based methods have emerged as an alternative where nanoscale features and elements are explicitly patterned followed by physical vapor deposition to deposit the metal, often at relatively lower temperatures. Examples include conventional electron beam lithography,[8] soft interference lithography,[9] and nanoimprint.[10] Yet, in general physical patterning methods yield two-dimensional (2D) nanostructures, often intended to emulate, or serve as models for, 3D features. Thus, chemical synthesis methods provide the best control over individual nanoparticle shape while physical methods are best for organizing the model nanoparticles over large areas. As a result, physical methods have evolved to include high-temperature processing to better tailor the morphology of individual nanoscale elements. Pattern liquefaction,[11] laser interference,[12] annealing,[13] nanomolding,[14] surface force driven assembly,[15] and pulsed laser-induced dewetting[16,17] have all emerged as integrated processes with lithographic methods. The nanosecond pulsed laser has proven especially useful for triggering the self and directed assembly[18] of patterned nanostructures.[19] Presented here is the directed liquid phase assembly of hierarchically arrayed nanoparticles on surfaces using a combination of electron beam lithography and pulsed laser melting. The term hierarchical is used here as in ref 20 where a series of sequential, self-assembly processes takes place; one level of self-assembly guides the next.

Liquid phase thin film dewetting has recently attracted much interest as a method to yield a spatially correlated metal particle network on a surface.[21−23] Spontaneously evolving surface waves on liquid metal films are either stable, leading to film smoothening, or unstable, leading to film fragmentation and resulting in the formation of particles. While this process involves a complex interplay between the laser melting (laser absorption depth and metal heating/melting) and the resultant liquid surface energies and viscosity, which dictate the nanocap wetting angle and perturbation growth rate, respectively, the process is generally applicable to metal/substrate systems where the metal has a lower melting point than the underlying substrate. Conveniently, pulsed laser melting at visible and ultraviolet frequencies favors the formation of nanosized

Received: November 6, 2013
Revised: December 19, 2013
Published: December 27, 2013

   dx.doi.org/10.1021/nl404128d | *Nano Lett.* 2014, 14, 774–782

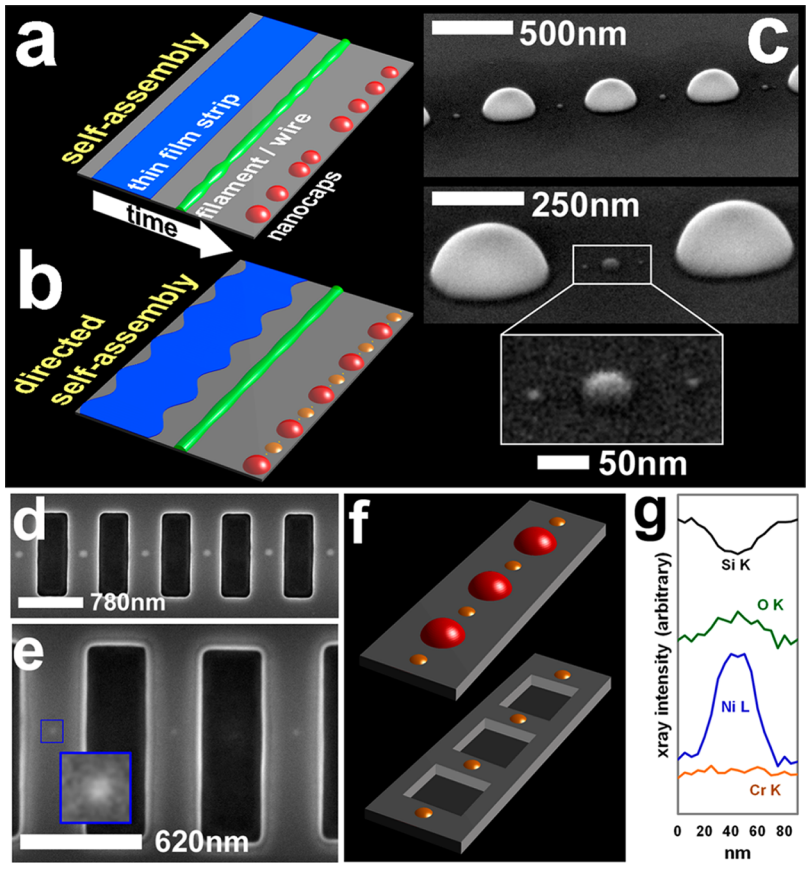

Figure 1. (a) A schematic illustration of the time evolution of thin film strip (TFS) melting. In the self-assembly case, the initial solid metal TFS has a straight edge (blue). A large area laser pulse (relative to the TFS size) irradiates and melts the strip at normal incidence. Liquid retraction ensues forming a fluid filament (green). A multitude of varicose modes develop on the filament surface as dictated by their wavelength. Fragmentation at surface wave troughs leads to the formation of droplets (red). Droplets resolidify as spherical nanocaps. (b) In the directed assembly case, a prescribed mode, defined by an amplitude and wavelength, is included on the strip edge. In this case, melting leads to the formation of a filament with a single mode. (c) Scanning electron microscopy images (52° capture angle) showing the fully developed Ni spherical nanocap ensemble at increasing magnification (top-to-bottom). The initial TFS dimensions were thickness (10 ± 1 nm) and average width (1 ± 0.015 μm). The synthetic edge perturbation had an amplitude of (75 ± 15 nm) and wavelength of 720 nm. Ten KrF (248 nm) pulses facilitated filament formation, breakup, and Ni spherical cap formation. (d) The focused ion beam (FIB) facilitated removal of the primary spherical nanocaps leaving behind a periodic array of rectangular depressions (dark, vertical rectangles). (e) The outcome of the same procedure applied to the droplets derived from initially smaller synthetic perturbation. (f) An illustration of the substrate before and after FIB processing. (g) A 25 nm semi-infinite Cr thin film was used to protect the Ni caps and substrate from Ni redeposition during FIB milling. Following Cr layer removal by wet etching, energy dispersive spectroscopy revealed negligible Cr contamination on the surface as well as preserved Ni nanocaps.

droplets for initial film geometries compatible with current nanolithography methods. For example, sub-20 nm initial solid metal film thicknesses absorb nearly all of the incoming light at these wavelengths thereby concentrating the energy in the film. Nanosecond laser pulses lead to nanosecond liquid metal lifetimes during film fragmentation into droplets. Rapid cooling rates preserve the droplet geometry while leaving negligible time for undesired evaporation or droplet migration by surface diffusion.

The Rayleigh–Plateau (RP) type of instability develops in liquid wires/filaments[24−26] while the spinodal type of instability is relevant for planar films. In both cases, numerous forces interact to influence instability development (Supporting Information). These instabilities are often considered within the framework of the long wave (LW) (also known as lubrication) approximation to the Navier–Stokes equations under conditions of a filament or droplet exhibiting small contact angles and negligible inertial effects. LW approach is known to capture many morphological aspects of instability development.[27] In particular, a useful insight is reached by considering the linear stability analysis (LSA), which is appropriate for the initial stages of instability development. This approach predicts a fastest growing surface mode (λ_m) where the growth rate spectrum for all possible modes (referred to as the dispersion curve) exhibits a broad distribution. In particular, stability of a long fluid strip with a truncated cylindrical geometry resting on a horizontal partially wetting substrate (the filament geometry) is of interest here. However, owing to relatively large contact angle (69 ± 8°) for liquid Ni on solid SiO_2, and the potential for non-negligible inertial effects following filament fragmentation,[28] it is unclear whether LW predictions are sufficiently accurate; for this reason we also carry out the volume-of-fluid (VoF) type of simulations. The VoF has several advantages relative to the LW theory such as removing the constraint of a small filament/droplet contact angle while making it possible to simulate fully 3D liquid flows. In the present work, we will combine the LSA based on the LW approach and VoF to gain better insight into the filament breakup.

dx.doi.org/10.1021/nl404128d | Nano Lett. 2014, 14, 774−782

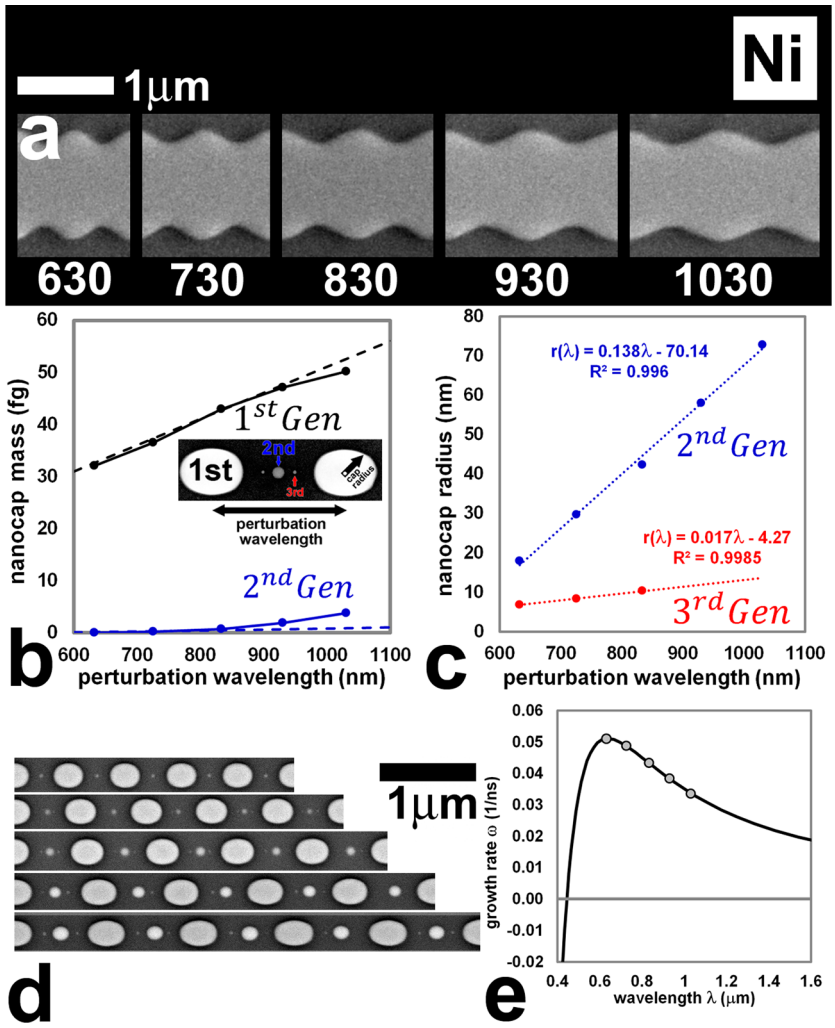

Figure 2. Synthetic perturbations make it possible to affect minute changes in nanoparticle size by using a more course, microscale "lever". (a) SEM images of five select Ni thin film strips (6 nm thick) showing ×2 perturbation periods. The perturbation wavelength is labeled for each case (nm). (b) Resolidified Ni nanocap mass as a function of the perturbation wavelength. Experiments are indicated by data points and solid lines. VoF simulation results are indicated by the hatched lines. (c) Final nanocap contact radius as a function of the initial perturbation wavelength for the second and third generation nanocaps. Linear fits reveal the sensitivity of the smallest nanocap sizes to much larger changes in the imposed perturbation wavelength. (d) The steady-state morphology that results following 10, 220 mJ/cm^2 KrF 18 ns laser pulses (compare with the initial strip dimensions shown in panel a). (e) Linear stability analysis makes it possible to predict the anticipated growth rate and hence breakup time for each wavelength based on the average filament dimension. Although the growth rates differ for each case, the cumulative liquid lifetime ensured that breakup was complete for all cases.

Figure 1a summarizes the specific case of the self-assembly of metallic nanoparticles via the RP instability. Briefly, liquid collects at the peaks of the fastest growing unstable modes. Liquid fragmentation occurs in the troughs. Following resolidification, nanoparticles lie at the peaks of the fastest growing mode. We use the terms nanoparticle and nanocap interchangeably as the final geometry is often a nanoscale, spherical cap but often referred to in the literature as a nanoparticle. The spacing between nanoparticles is expected to be comparable to λ_m. Yet, nanoparticle spacing is somewhat variable because a host of modes have comparable growth rates to λ_m and therefore develop as well.

The growth of any given mode is exponential in the early stages of development. As a result, an infinitesimal advantage in the magnitude of the initial amplitude of a mode may lead to a significant advantage in evolution later. This is the key step for the directed assembly approach.[16,28] For example, we have demonstrated that filament fragmentation can be dominated by a single mode if imposed on the filament at the early stages of development. Figure 1b shows a schematic of this process and Figure 1c the experimental results.[16] Here, it is of interest to understand the advanced temporal stages of instability development in the nonlinear regime when filament breakup occurs. In this regime, the LSA mentioned above can provide only a guidance since it does not apply as the perturbation amplitudes become comparable to the filament radius, and therefore to understand this stage of instability we will resort to numerical simulations. Clearly, this nonlinear stage of instability development is crucial because an organized process of nanoparticle formation, which is very attractive for controlled nanoparticle formation on surfaces, occurs during this stage. Thus, understanding filament breakup could potentially lead to a new lithography paradigm for implementing nanoparticle based technologies.

Here, we present results indicating that the order originally imposed during directed assembly transcends beyond the

dx.doi.org/10.1021/nl404128d | Nano Lett. 2014, 14, 774−782

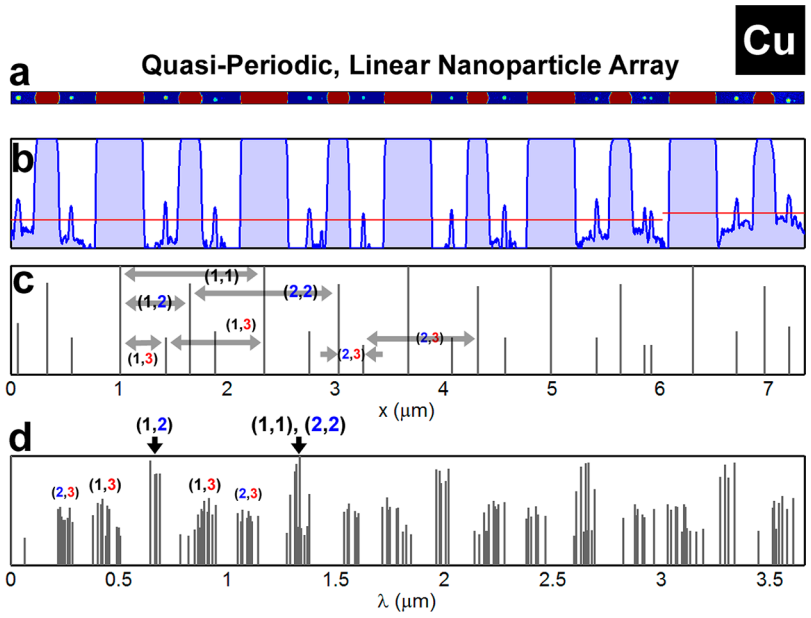

Figure 3. (a) A partially cropped SEM image showing a top down image of a quasi-periodic, self -similar Cu nanoparticle array (the original image is shown in (Supporting Information, Figures S3−S5). The Cu nanoparticle array was formed from a TFS with a 1.3 μm synthetic edge perturbation, a thickness of 9 nm, and an average width of 1 μm. (b) The linear image intensity profile following the summation of the SEM image intensity in the row-direction in the image (blue profile). The red line delineates the specified intensity threshold used to find individual nanocaps. (c) The mean position of each cap is represented by a vertical spike; the length of the spike is proportional to the cap width derived from (b). The intensity profile is raised to the 5th root $I(x)^{1/5}$ which provide a clear indication of the satellite generation based on the spike height. The superimposed arrows indicate the various cap spacings as well as the generation of caps shown in parentheses. (d) The spatial autocorrelation function (SACF, Supporting Information) of the data set shown in (c).

perturbation wavelength of ∼1 μm down to much smaller length scales ∼10 nm. As the liquid lifetime increases, smaller filaments develop between evolving droplets and a self-similar process emerges whereby smaller droplets form at accelerated rates. Remarkably, the results presented here indicate that the nanocap radius may be dictated at sub-20 nm length scales with a precisely predictable spatial location. Control of the size of substrate supported nanoparticles is critical both for their future applications, for example, plasmonics,[29] as well as amenability to testing and characterization using emerging scanning probe methods.[30] Thus, the ability to isolate the smallest spherical nanocaps, following the self-assembly process, is important. This was demonstrated using conventional focused ion beam milling (see Figure 1d−g) by selectively removing only the primary nanocaps from the substrate surface (Supporting Information).

Results (Morphology). In the discussion that follows, the spherical caps are studied in terms of their temporal generation. Initially, prerequisite liquid bulges begin to form at the peak positions of the original thin film strip (TFS), forming a perturbed filament. After breakup, we refer to these as the primary or first generation caps. As will be shown below, evidence suggests that second generation nanocaps, that is, satellites, form from the liquid contained in the smaller fine filament that spans the primary bulges. In time, primary droplets formed first, followed by fine filament evolution and then satellites. Third generation and even fourth generation nanocaps were observed leading to a hierarchical, quasi-periodic array of nanoparticles. Regarding the metallic materials explored, experiments were conducted using single component metals (Ni and Cu) as well as binary materials including Ni−Cu and Ni−0.2Fe (permalloy). The substrate was always SiO_2. These materials have attracted recent interest with regards to magnetic−plasmonic interactions,[31] core shell nanomagnetic properties,[32] conducting nanowire networks,[33] and spin valves[34] where ordered ensembles of nanoparticles or nanowires are relevant.

A systematic study of the influence of the initial perturbation wavelength on the final nanocap size was carried out in order to determine how accurately and precisely the final nanocap size and spacing could be controlled. Figure 2 shows the results of a study carried out over an unstable wavelength range of 630−1030 nm where fragmentation into droplets is always expected. Figure 2a shows SEM images of ×2 TFS periods for the select perturbation wavelengths (superimposed, units of nanometers) used to carefully analyze (1) the Ni composition, as well as (2) the average and variation in final nanocap size. The Ni TFSs were 6 ± 1 nm thick. The strips were exposed to ×10, 18 ns KrF laser pulses leading to the spherical cap geometries shown in Figure 2d. Nanocap mass versus the initial perturbation wavelength is shown in Figure 2b for various nanocap generations. Nanocap size was characterized by the contact radius of the cap (r_c) with the underlying substrate and represented as the y-axis in Figure 2c. The relationship between the generation of the cap, the initial perturbation wavelength, and the final nanocap radius is color coded and shown in the inset in Figure 2b

A linear relationship was revealed between the TFS perturbation wavelength and final nanocap radius for all cap generations (at least within experimental error of cap contact width that is reported later). A linear relationship between these variables is an advantageous result from a practical standpoint because it enables controlled directed assembly for creating, for example, accurately sized micro/nanoelectronic compatible nanoparticle arrays. Moreover, as Figure 1d−f shows, selected generations can later be removed from the

dx.doi.org/10.1021/nl404128d | Nano Lett. 2014, 14, 774−782

linear array in order to select a specific generation for use. Lastly, (Supporting Information, Figure S1) demonstrates that a high density of variable-sized nanocaps may be produced along a single TFS by modulating the perturbation wavelength along the length of the TFS.

Figure 2c presents a magnified view of the contact radius versus perturbation wavelength (shown in Figure 2b) in order to better reveal the results of the linear fit to the second and third generation nanocaps. The slope of the linear fits ($dr_c/d\lambda$) provides a measure of the sensitivity of the perturbation wavelength (λ) as a switch to control the final nanocap contact radius (r_c) of the nanoparticles

$$\left.\frac{dr_c}{d\lambda}\right|_{2nd} = 0.14, \quad \left.\frac{dr_c}{d\lambda}\right|_{3rd} = 0.02 \qquad ([1])$$

The implications of these expressions are most notable for photolithographic applications where it becomes possible to create arrays of sub-20 nm, evenly-spaced nanocaps while using visible wavelengths for pattern exposure of the initial perturbation wavelength. The high spatial fidelity of the cap formation process may be seen in Figure 2d.

The LSA prediction of filament stability and the liquid lifetime per laser pulse of the metal filaments is discussed in more detail in (Supporting Information). Multicomponent metals are also compatible with the satellite droplet formation process, and this is important from the standpoint of creating functional nanomaterials. The (Supporting Information, Figure S2) also provides a summary of results for the binary pairs of Ni/Cu and Ni/Fe

Results (Nanocap Spatial Alignment). The physical process of filament destabilization and breakup preserves the spatial fidelity of the initial nanoscale synthetic perturbation;[16] first generation caps are accurately centered at the peaks of the initial TFS edge perturbation. However, the precision in second generation cap position with respect to the half-wavelength ($\lambda/2$) position exhibits variation. In order to evaluate the spatial registration of the second generation caps with respect to the first generation caps, spatial autocorrelation functions (SACF)[35] were calculated. The procedure for deriving the SACF is described in (Supporting Information, Figures S3–S5). Figure 3b shows a secondary electron image intensity cross-section along 6 periods of a Cu spherical cap array formed from a TFS with a thickness of ~9 nm, a width of 1 μm, and a synthetic perturbation wavelength of 1.3 μm. Nanocap formation was achieved using a laser fluence of 180 ± 10 mJ/cm^2 in a sequence of 10 laser pulses. Briefly, the SACF operates on a digital array of spikes resembling delta functions (Figure 3c) where the position of each spike represents the mean position of a spherical cap. The intensity of a spike is proportional to the cap generation. The spacings between selected spherical caps are identified in Figure 3c for clarity using parenthesis where the integer specifies the generation. The generation color matches the color scheme used in Figure 2b–c. The SACF is provided in Figure 3d. The SACF clearly reveals the spatial ordering of the second generation caps with respect to the first generation, that is, labeled (1, 2), by the clustering of spikes at $\lambda/2$. This self-similarity transcends to the third cap generation where the n^{th} generation cap is surrounded by two adjacent $(n + 1)$th generation caps. The SACF result is akin to a linear modulated, quasi-crystal array were intensity modulation reflects the period in contact radius superimposed with the period of spatial array.[36]

SACFs acquired over a single wavelength made it possible to quantify the second generation cap spatial registration by the splitting of the (1,2) SACF $\lambda/2$ peak position (Supporting Information). Specifically, the SACF peak splitting revealed the precision in placement of the second generation cap with respect to the half-wavelength position between first generation caps. (Supporting Information, Figure S6) reveals a standard deviation of 9 nm for the splitting measured between five independent, second generation Ni nanocaps. Because the initial synthetic perturbation wavelength is 830 nm, this finding shows that the placement of second generation caps is accurate to about 1%.

Results (Composition). X-ray energy dispersive spectroscopy (XEDS) was used to verify the metal content of the nanocaps. XEDS results confirmed metallic purity for the first and second generation satellites for the case of Ni (Supporting Information, Figures S7–S9). A smaller oxygen characteristic peak was also observed suggesting the anticipated NiO sheath surrounding the cap (Figure 1g). The standard deviation in second generation spherical cap size was also estimated using XEDS. For example, the standard deviation in contact width for the 680 nm perturbation was ±6 nm while the deviation was ±7 nm for the 780 nm perturbation. Monte Carlo simulations of electron scattering trajectories in model spherical nanocaps were used to confirm the validity of using XEDS to estimate the nanocap width (Supporting Information, Figure S10).

Results (Computational). Further insight regarding filament breakup and satellite formation can be obtained by computations. Here we utilize VoF simulations described briefly in Methods and more extensively in Supporting Information. Figure 4 shows the fluid thickness before, at, and after the breakup for 600 and 1000 nm wavelengths of imposed perturbation. We see formation of a thin filament between the primary drops: the point where this filament

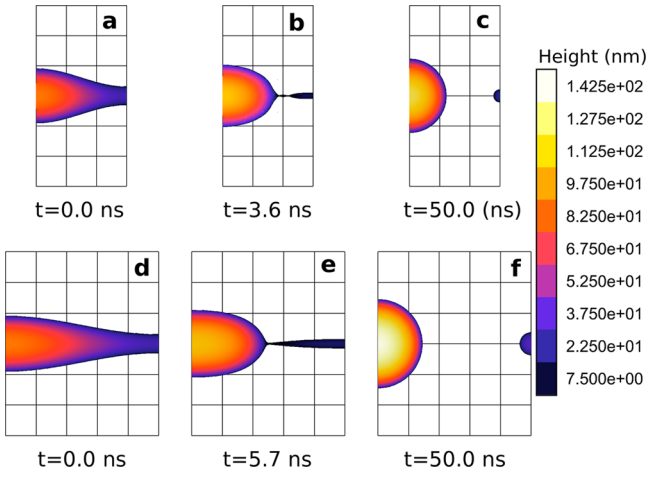

Figure 4. Computational (VoF) results showing evolution of a Ni filament perturbed by either 600 nm wavelength perturbation (a–c) or 1000 nm perturbation (d–f). Only one-half of the period is shown so that there is a vertical line of symmetry at both left and right boundaries of the computational domain. The parts (b) and (e) show the times just before the breakup takes place; note that the breakup happens faster for the shorter perturbation. The color scheme shows the thickness of the fluid in nanometers. The length of each square box in the figure is 100 nm, showing that the breakup happens further away from the right boundary for the longer perturbation wavelength, leading eventually to larger satellite drops.

dx.doi.org/10.1021/nl404128d | Nano Lett. 2014, 14, 774–782

breaks depends on the distance between the primary drops; the filament is longer for larger distances. Consequently, the breakup points are also shifted to larger distances, and therefore larger secondary drops result for larger distance between the primary drops. This trend is consistent with the experiments. The simulation results for the dependence of the satellite drops final mass on the perturbation wavelength are also shown in Figure 2b. The simulation results are in agreement with experimental results for the smaller perturbation wavelengths studied (λ = 630−830 nm). At larger perturbation wavelengths, the simulations predicted larger primary drops at the sacrifice of mass derived from the second generation nanocaps. This discrepancy is most likely due to variations in the experimental wetting angle observed for larger caps (r_c > 200 nm) tend to have θ > 70. It should be also noted that the simulations are currently limited to considering θ = 90 and for this reason we do not show radii of the drops resulting from simulations in Figure 2c, since the comparison with the experimental values would be misleading. As further discussed in Supporting Information, Figure S11, another factor influencing the size of satellite drops is the slip length, β. In the present work, we use β = 60 nm, consistent with ref 37; smaller β yields larger satellite drops. Considering spacing of satellite drops, we find that, consistent with experiments, the center to center spacing between first and second generation droplets is $\lambda/2$.

Figure 5, showing the pressure in the fluid, provides additional insight regarding the process of breakup itself; the

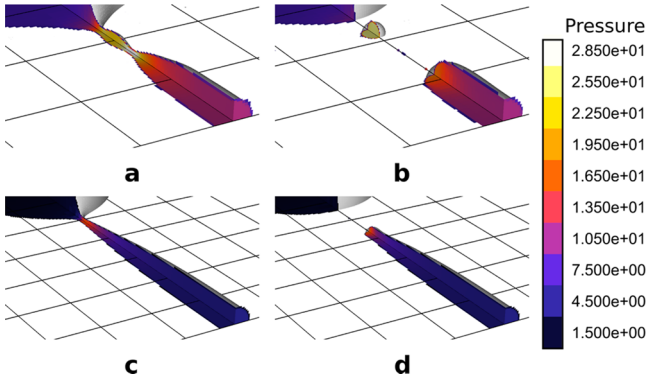

Figure 5. Pressure inside of the Ni fluid at the moment of breakup for 600 nm (a,b) and 1000 nm (c,d) perturbation wavelengths. The main drop is shown on the left, and the filament that breaks off is on the right. For longer times, the filaments collapse to satellite drops. The pressure is scaled by the reference pressure, which is taken as the (capillary) pressure in the unperturbed filament. The length of each square box in the figure is 100 nm.

animations are also available as a part of (Supporting Information). We see (particularly clearly in the animations) that capillarity driven contraction of the main body of the fluid leaves behind a filament and at the point where filament connects with the main drop, a large pressure starts to develop due to the increased curvature there. This large pressure leads to a breakup and formation of a satellite drop. We note that the simulations capture only first and second generation of droplets, although in some simulations, such as the one shown in Figure 5a,b, further breakups may occur. However, the additional smaller drops that form merge with the larger ones (the main drop in the example shown in Figure 5a,b), in contrast to the experiments. We discuss this difference between the Simulations and Experiments below.

Discussion. Experimental demonstration of satellite droplet formation for fluids deposited on surfaces is very limited, and as far as we are aware, this is the first work reporting formation of these structures on the nanoscale. Similar satellite drop formation has been reported in recent experiments carried out with PDMS filaments on the macroscale.[38] These results were later discussed in,[39] where the mechanism for breakup and formation of generations of satellite drops on the level of LW theory was proposed.

The prerequisite to satellite droplet formation is a fine filament extending between the primary bulges of liquid metal. The position of these initial bulges is set by the imposed synthetic perturbation on the original TFS. For example, a transient morphology between the original TFS and filament may be seen in Figure 6a for the case of Ni experiments or in

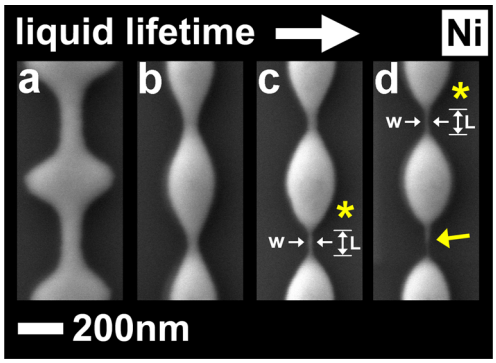

Figure 6. The temporal development of Ni caps from the thin film strip geometry. The initial TFS geometry for this case was λ = 600 nm, w = 1 μm and h = 10 nm. The laser fluence was 220 mJ/cm^2 and 5 laser pulses were applied to the sample. (a) TFS contraction to filament formation is nearly complete. (b) The prescribed perturbation is growing on the filament consistent with the unstable growth rate prediction for this case. (c−d) Further development leads to the formation of filaments between the forming, first generation drops. The fine filaments shown extending between the primary bulges are a characteristic precursor morphology to satellite droplet formation with characteristic dimensions of the length (L) and contact width (w). Rapid resolidification makes it possible to freeze transient morphologies such as these fine filaments. The total liquid lifetime effectively increases from left-to-right, (1) approaching filament formation, (2) perturbed filament, and (3−4) partial breakup showing the emergence of a small, secondary filament between the primary Ni droplets.

Figure 4 in simulations. Further development ultimately leads to a perturbed, or undulated, filament (Figure 6b). Careful inspection of Figure 6b reveals that the fluid bridges extending between the primary bulges have varying widths. This variability results from "macroscopic" noise sources such as TFS surface roughness, spatial fluctuations in laser intensity, among others. Subsequently, these experimental results reveal that the fluid bridges undergo thinning as the filament attempts to reduce surface area forming the prerequisite fine filament (Figure 6c).

Yang and Homsy[39] have provided predictions for the time and length scales for the filament geometry prior to breakup. Specifically, in ref 39 a relationship between the length of the primary filament length (L) and its half width (a_c) of L/a_c = 8.886 [ref 39 Table I] is found. The Ni filaments shown in Figure 6c,d (indicated by yellows asterisks) yield two pairs of (L,w) estimates of (90 nm, 20 nm) and (105 nm, 24 nm). The

dx.doi.org/10.1021/nl404128d | Nano Lett. 2014, 14, 774−782

resulting L/a_c ratios for these two cases are 9 and 8.75, which are in excellent agreement with the ratios mentioned above.[39] Yet, we should note that in ref 39 actual breakup was not considered, just an approach to it. However, their results suggested the initial formation of secondary and even tertiary drops and the existence of a possible cascade (a fact observed in the experiments[38]).

Further insight can be reached by considering a problem of breakup of a free-standing liquid jet. This rupture process that also leads to formation of satellites droplets has been analyzed from experimental, computational, and theoretical points of view, see refs 26 and 40 for extensive reviews. While this problem is somewhat different from the one considered here, we expect that the breakup mechanism and the satellite drop formation have some common features in both cases.

The analysis of the jet problem shows that close to breakup the behavior of the fluid is self-similar and therefore it should be essentially independent of the initial conditions. Furthermore, it is found that differences are expected during the breakup if inertial effects are important.[26,40] To analyze the possible relevance of inertia for the experiments considered here, we give in Table 1 the various length and time scales relevant to the geometries presented in Figure 6. Notably, the Ohnesorge number (Oh) of 0.3 indicates that inertial effects may play a role at the length and time scales associated with the fine filament connecting primary drops,[41] while at larger length scales, such as those characterizing the initial filament, viscosity effects dominate both fluid flow and instability development. Specifically, for Oh < 1, a rapidly retracting filament is predicted to form following breakup.[42] Clearly such an event would affect final nanocap size and position of secondary and subsequent droplets. This suggests that inertial effects are important during instability development and satellite formation.

Table 1. The Various Length and Time Scales Relevent to the Development of the Liquid Ni Rivulet, as Well as the Fine Filament that Connects the Primary Bulges, during Initial Instability Development for the Case of a Rivulet Supported on an Atomically Flat SiO_2 Surface

l_{obs}	observation length scale (SE^1 electron probe)	20 nm	
Oh	Ohnesorge number (primary filament width)	0.3	$\eta/(\gamma\rho w)^{1/2}$
l_η	liquid filament/bridge	1 nm	$\eta^2/\gamma\rho$
t_η	liquid filament/bridge	2.6 ps	$\eta^3/\gamma\rho^2$
l_T	thermal capillary length/stochastic length scale	1 Å	$(k_BT/\gamma)^{1/2}$
λ	synthetic perturbation wavelength(s)	1 μm	
A_0	synthetic perturbation amplitude	50−100 nm	
w	primary filament width	10 nm	
a_c	primary filament height	10 nm	

γ = surface tension (1.781 N/m), η = viscosity (0.004 Pa.s], k_B = Boltzmann's constant, T = temperature (1650 K, melting temperature) and ρ = density (7900 kg/m^3, liquid phase).

The investigations of the jet problem have also suggested the importance of thermal fluctuations, or "microscopic" noise[41] at the smallest scales. For example, the addition of a weak noise source to the hydrodynamic equation has reproduced the experimental observation of iterated fine filament thinning (ref 41 Figure 1b). Such iterated thinning is also present in our experiments, see Figure 6d (yellow arrow), and in some simulations (see Figure 4b). Thus, the subsequent formation of satellite droplets may arise from thermal fluctuations as the fine filament width approaches the stochastic capillary length scale, see Table 1. Thermal fluctuations relaxing on atomically thin polymeric films have been investigated with regards to film stability.[43] The relevance of such fluctuations in a jet problem was confirmed by recent molecular dynamics based simulations.[44,45] Specifically, the self-similarity of primary, secondary and tertiary filament production is found to be disrupted at the nanometer scale as the surface tension and viscosity properties fluctuate along the filament.[44] A simple interpretation of the influence of thermal noise is that thinning fluctuation of amplitude $-\Delta r$ in the narrow portion of a filament has a bigger net effect than a thickening fluctuation of $+\Delta r$ in a thick portion of the filament.[46] Thus, transverse pressure gradients favoring breakup are accelerated while axial gradients favoring smoothening are negligibly impacted. The net effect of this process is a more favored filament breakup.

The preceding discussion may also help us understand some differences between the experimental and computational results. By comparing Figure 4 and Figure 6, we see that the primary breakup mechanism is very similar between the simulations and experiments. Moreover, the second generation nanocaps in simulations are located at $\lambda/2$, as in most of the experiments. However, the filament that forms as a result of breakup in simulations collapses eventually to single, central (satellite) drop, typically without further breakup. We note that we have carried out simulations with superimposed perturbations of the filament shape and also have not seen any additional breakup, suggesting that a noisy initial condition due to, for example, perturbed filament shape, is not enough to yield tertiary and higher droplets. The problem of millimetric and submillimetric filaments on substrates has also been studied with a diffuse boundary approach[47] showing, as in our case, the formation of secondary drops but not yielding tertiary ones. The fact that our experiments do observe breakup, leading to tertiary and even higher order drops for small perturbation wavelengths could be a consequence of a series of effects that require further study. Tertiary drops could arise from a process of cascade to smaller scales.[39] New models that deal with these scales might require the study of stochastic effects caused by thermal fluctuations[45] and a more detailed description of the liquid−solid interaction forces allowing for thickness dependent liquid film energy in the computational framework. Our research in these directions is ongoing.

Methods. *Experiments. Nanosecond Pulsed Laser Irradiation.* The thin film strips were irradiated at normal incidence. The total surface array occupied by the strips on the substrate surface was ~10^5 μm^2. The KrF (248 nm) pulsed laser beam covered a surface area of ~10^7 μm^2. The relatively larger size of the incident laser pulse ensured that each strip was irradiated with uniform laser fluence. Ni nanoparticles were performed using (5−10) sequential laser pulses each with a fluence of 220 mJ/cm^2. Cu spherical caps were formed using 180 mJ/cm^2 (10 pulses), Ni−Cu caps with 200 mJ/cm^2 (5 pulses) and finally Ni−0.2Fe caps with 200 mJ/cm^2 (5 pulses). The laser pulse width (~18 ns) was significantly less than the time between pulses (100 ms). This led to noninteracting laser pulses, that is, the sample transiently melted, resolidified, and returned to room temperature prior to the next laser pulse. Moreover, the massive rate of heating and cooling (~10^8 K/s) makes transient phenomena, such as solid-state mass transport and oxidation, negligible. As a result, the total liquid lifetime accumulated

dx.doi.org/10.1021/nl404128d | Nano Lett. 2014, 14, 774−782

using multiple laser pulses leads to the same morphological result as one laser pulse yielding the equivalent liquid lifetime. Simulation results of the time−temperature profile per pulse for the initially flat Ni film, for example, 26 ns for 6 nm Ni film, are on the order of the predicted breakup times provided by LSA (Figure 2e). These predictions were consistent with the fact that experimentally observed breakup was complete in both cases after two laser pulses. The details of the time−temperature simulation are presented in ref 16.

Nanofabrication (Thin Film Strip Definition). Thin film strip definition and deposition was accomplished using electron beam lithography, DC magnetron sputtering, and a solvent facilitated lift-off process, the details of which are provided.[28] The Ni thin film strip patterns were exposed into an electron sensitive resist coated on 100 nm SiO_2/Si wafers. Specifically, a poly(methyl methacrylate) (PMMA), positive tone electron sensitive resist (495-A4, Shipley) was spin coated using a wafer rotation speed of 4000 rpm for a total of 60 s. Following resist application, an elevated temperature bake was performed at 180 °C using a conventional hot plate. Pattern generation in the resist was performed using a Raith Elphy Quantum software package that communicated with an FEI Nova 600 dual electron/ion microscope via a beam blanker. A focused electron probe with an 18 keV landing energy and 160 pA beam current was used to expose the TFS resist patterns. The TFS patterns were exposed using a rectangular scanning grid with a 20 nm exposure step. An exposure dose of 300 $\mu C/cm^2$ was required to yield fully activated TFS patterns for later resist development. Subsequent resist development was carried out by submerging the resist-coated wafer in a solution of 1:3 methyl isobutyl ketone (MIBK)/isopropyl alcohol (IPA), respectively, for 100s. An IPA rinse was conducted after removing the wafer from the MIBK/IPA bath and blown dry with dry N_2 gas. The final step in preparation for metal deposition was an oxygen plasma treatment performed in order to remove residual resist from the exposed TFS patterns. Specifically, an 8 s exposure of the resist-coated wafer to an oxygen plasma generated in a reactive ion etcher using a power setting of 100 W to sustain a capacitively coupled plasma. An oxygen flow rate of 10 cm^3/min was used with a constant chamber pressure setting of 150 mTorr. Regarding metal sputtering, initial thin film strip thicknesses ranged from 6−10 nm for all reported experiments and are indicated in the appropriate figure captions. In general, sputtering rates of ∼5 nm/min were used to deposit the films of Cu, Ni, Ni−0.2Fe, and Cr. The sputtering was conducted using the DC magnetron method under constant power deposition mode at 30 W. A constant chamber pressure of 3 mTorr Ar was maintained during sputtering and the target-to-substrate distance was ∼4−5 cm. The Ar gas flow rate was 25 cm^3/min.

Nanofabrication (Chromium Masking and Ion Milling). These experimental details are provided in Supporting Information.

Energy Dispersive Spectroscopy. These experimental details are provided in Supporting Information, Figures S7−S9.

Simulations. Volume-of-Fluid Simulations. We model the breakup of the nanostructures by treating the dynamics using the two-phase Navier−Stokes equations (Supporting Information). Briefly, the metal is assumed to be in fluid state for the entirety of the simulation time, ignoring the effects of solidification. We perform simulations using a VoF-based solver, implemented in an open source software package.[48] The details of this solver are described in ref 49 and some further details are given in Supporting Information.

■ ASSOCIATED CONTENT

Ⓢ Supporting Information

Details related to additional experimental results, image processing and analysis, energy dispersive spectroscopy, and the volume of fluids simulation method. This material is available free of charge via the Internet at http://pubs.acs.org.

■ AUTHOR INFORMATION

Corresponding Author

*E-mail: fowlkesjd@ornl.gov

Notes

The authors declare no competing financial interest.

■ ACKNOWLEDGMENTS

Y.W. and J.D.F. acknowledge support from the U.S. Department of Energy, Basic Energy Sciences, Materials Science and Engineering Division for sponsoring the aspects of this work related to understanding the fundamental mechanisms operative during liquid phase, thin film dewetting. A portion of this work related to the deposition of thin films and nanolithography was conducted at the Center for Nanophase Materials Sciences, which is sponsored at Oak Ridge National Laboratory by the Scientific User Facilities Division, Office of Basic Energy Sciences, U.S. Department of Energy. P.D.R. acknowledges support from NSF Grant CBET-1235651. L.K. acknowledges support by NSF Grant CBET-1235710. J.A.D. and A.G.G. acknowledge support from Consejo Nacional de Investigaciones Científicias y Técnicas (CONICET, Argentina) with Grant PIP 844/2011.

■ REFERENCES

(1) Cuenya, B. R. *Thin Solid Films* **2010**, *518* (12), 3127−3150.
(2) Billas, I. M. L.; Chatelain, A.; Deheer, W. A. *Science* **1994**, *265* (5179), 1682−1684.
(3) Zhang, Z.; Li, J. C.; Jiang, Q. *J. Phys. D: Appl. Phys.* **2000**, *33* (20), 2653−2656.
(4) Alivisatos, A. P. *J. Phys. Chem.* **1996**, *100* (31), 13226−13239.
(5) Moshfegh, A. Z. *J. Phys. D: Appl. Phys.* **2009**, *42* (23), 233001.
(6) Beliatis, M. J.; Martin, N. A.; Leming, E. J.; Silva, S. R. P.; Henley, S. J. *Langmuir* **2011**, *27* (3), 1241−1244.
(7) Atwater, H. A.; Polman, A. *Nat. Mater.* **2010**, *9* (3), 205−213.
(8) Pasquale, A. J.; Reinhard, B. M.; Dal Negro, L. *ACS Nano* **2011**, *5* (8), 6578−6585.
(9) Henzie, J.; Lee, M. H.; Odom, T. W. *Nat. Nanotechnol.* **2007**, *2* (9), 549−554.
(10) Chou, S. Y.; Krauss, P. R.; Renstrom, P. J. *Science* **1996**, *272* (5258), 85−87.
(11) Chou, S. Y.; Xia, Q. F. *Nat. Nanotechnol.* **2008**, *3* (6), 369−369.
(12) Tan, C.; Peng, C. S.; Pakarinen, J.; Pessa, M.; Petryakov, V. N.; Verevkin, Y. K.; Zhang, J.; Wang, Z.; Olaizola, S. M.; Berthou, T.; Tisserand, S. *Nanotechnology* **2009**, *20* (12), 125303.
(13) Ye, J.; Thompson, C. V. *Adv. Mater.* **2011**, *23* (13), 1567−1571.
(14) Kumar, G.; Tang, H. X.; Schroers, J. *Nature* **2009**, *457* (7231), 868−872.
(15) Leong, T. G.; Zarafshar, A. M.; Gracias, D. H. *Small* **2010**, *6* (7), 792−806.
(16) Fowlkes, J. D.; Kondic, L.; Diez, J.; Wu, Y. Y.; Rack, P. D. *Nano Lett.* **2011**, *11* (6), 2478−2485.
(17) Xia, Q. F.; Chou, S. Y. *Nanotechnology* **2009**, *20* (28), 285310.
(18) Kumar, P. *Nano. Res. Lett.* **2010**, *5* (9), 1367−1376.
(19) Henley, S. J.; Carey, J. D.; Silva, S. R. P. *Appl. Surf. Sci.* **2007**, *253* (19), 8080−8085.

(20) Lopes, W. A.; Jaeger, H. M. *Nature* **2001**, *414* (6865), 735−738.
(21) Krishna, H.; Shirato, N.; Favazza, C.; Kalyanaraman, R. *J. Mat. Res.* **2011**, *26* (2), 154−169.
(22) Henley, S. J.; Beliatis, M. J.; Stolojan, V.; Silva, S. R. P. *Nanoscale* **2013**, *5* (3), 1054−1059.
(23) Mehrabian, H.; Feng, J. J. *J. Fluid Mech.* **2013**, *717*, 281−292.
(24) Rayleigh, L. *Philos. Mag. Ser. 5* **1892**, *34* (207), 145−154.
(25) Plateau, J. A. F. *Acad. Sci. Brux. Mem.* **1843**, *16*, 3.
(26) Eggers, J.; Villermaux, E. *Rep. Prog. Phys.* **2008**, *71* (3), 036601.
(27) Diez, J. A.; Gonzalez, A. G.; Kondic, L. *Phys. Fluids* **2009**, *21* (8), 082105.
(28) Fowlkes, J. D.; Kondic, L.; Diez, J. A.; Gonzalez, A. G.; Wu, Y. Y.; Roberts, N. A.; McCold, C. E.; Rack, P. D. *Nanoscale* **2012**, *4* (23), 7376−7382.
(29) Albella, P.; Garcia-Cueto, B.; Gonzalez, F.; Moreno, F.; Wu, P. C.; Kim, T. H.; Brown, A.; Yang, Y.; Everitt, H. O.; Videen, G. *Nano. Lett.* **2011**, *11* (9), 3531−3537.
(30) Kumar, A.; Ciucci, F.; Morozovska, A. N.; Kalinin, S. V.; Jesse, S. *Nat. Chem.* **2011**, *3* (9), 707−713.
(31) Valev, V. K.; Silhanek, A. V.; Gillijns, W.; Jeyaram, Y.; Paddubrouskaya, H.; Volodin, A.; Biris, C. G.; Panoiu, N. C.; De Clercq, B.; Ameloot, M.; Aktsipetrov, O. A.; Moshchalkov, V. V.; Verbiest, T. *ACS Nano* **2011**, *5* (1), 91−96.
(32) Johnston-Peck, A. C.; Wang, J. W.; Tracy, J. B. *ACS Nano* **2009**, *3* (5), 1077−1084.
(33) Rathmell, A. R.; Nguyen, M.; Chi, M. F.; Wiley, B. J. *Nano. Lett.* **2012**, *12* (6), 3193−3199.
(34) Bader, S. D. *Rev. Mod. Phys.* **2006**, *78* (1), 1−15.
(35) Pichler, S.; Bodnarchuk, M. I.; Kovalenko, M. V.; Yarema, M.; Springholz, G.; Talapin, D. V.; Heiss, W. *ACS Nano* **2011**, *5* (3), 1703−1712.
(36) Steurer, W.; Sutter-Widmer, D. *J. Phys. D: Appl. Phys.* **2007**, *40* (13), R229−R247.
(37) Roberts, N. A.; Fowlkes, J. D.; Mahady, K.; Afkhami, S.; Kondic, L.; Rack, P. D. *ACS Appl. Mater. Interfaces* **2013**, *5* (10), 4450−4456.
(38) Gonzalez, A. G.; Diez, J.; Gratton, R.; Gomba, J. *Europhys. Lett.* **2007**, *77*, 44001.
(39) Yang, L.; Homsy, G. M. *Phys. Fluids* **2007**, *19* (4), 044101.
(40) Eggers, J. *Rev. Mod. Phys.* **1997**, *69* (3), 865−929.
(41) Brenner, M. P.; Shi, X. D.; Nagel, S. R. *Phys. Rev. Lett.* **1994**, *73* (25), 3391−3394.
(42) Castrejon-Pita, A. A.; Castrejon-Pita, J. R.; Hutchings, I. M. *Phys. Rev. Lett.* **2012**, *108* (7), 074506.
(43) Willis, A. M.; Freund, J. B. *Phys. Fluids* **2010**, *22* (2), 022002.
(44) Moseler, M.; Landman, U. *Science* **2000**, *289* (5482), 1165−1169.
(45) Fowlkes, J.; Horton, S.; Fuentes-Cabrera, M.; Rack, P. D. *Angew. Chem., Int. Ed.* **2012**, *51* (35), 8768−8772.
(46) Eggers, J. *Phys. Rev. Lett.* **2002**, *89* (8), 084502.
(47) Ghigliotti, G.; Zhou, C.; Feng, J. J. *Phys. Fluids* **2013**, *25* (7), 072102.
(48) Popinet, S. http://gfs.sourceforge.net/wiki/index.php/Main_Page, 2012, 1.3.2.
(49) Popinet, S. *J. Comput. Phys.* **2009**, *228* (16), 5838−5866.